Glycerol plasticisation of chitosan/carboxymethyl cellulose composites: Role of interactions in determining structure and properties‡

Pei Chen [a,b], Fengwei Xie [b,c,*,†], Fengzai Tang [d], Tony McNally [b,**]

[a] *College of Food Science, South China Agricultural University, Guangzhou, Guangdong 510642, China*

[b] *International Institute for Nanocomposites Manufacturing (IINM), WMG, University of Warwick, Coventry CV4 7AL, United Kingdom*

[c] *School of Chemical Engineering, The University of Queensland, Brisbane, Qld 4072, Australia*

[d] *WMG, University of Warwick, Coventry CV4 7AL, United Kingdom*

[*] Corresponding author. Email addresses: d.xie.2@warwick.ac.uk, fwhsieh@gmail.com (F. Xie)

[**] Corresponding author. Email address: t.mcnally@warwick.ac.uk (T. McNally)

[†] This author leads the research.

‡ Supplementary material provided.

Abstract:

Biopolymers such as chitosan and cellulose continue to attract much interest as they have many appealing characteristics such as biodegradability, biocompatibility, chemical versatility and natural functionality; however, many of their properties usually require further tailoring for specific purposes. This study shows that glycerol plasticisation and the addition of graphene oxide (GO) or reduced graphene oxide (rGO) altered the properties of chitosan and a chitosan/carboxymethyl cellulose (CMC) blend. For the chitosan/CMC matrix, GO or rGO was likely to disrupt polyelectrolyte complexation (PEC) between the two biopolymers, leading to weakened mechanical properties and increased surface hydrophilicity. Conversely, glycerol assisted PEC by increasing the biopolymer chain mobility, leading to reduced surface hydrophilicity. Moreover, some synergistic effects from a combination of glycerol and GO/rGO were evident. Specifically, GO/rGO notably increased the toughness of the chitosan film on inclusion of 40 wt% glycerol. Both GO and rGO reduced the relaxation temperatures of the chitosan/CMC film with 20 wt% glycerol added, resulting in increased biopolymer chain mobility. Moreover, the bionanocomposites showed high relative permittivity (54–387). Thus, this work describes how complex interactions in multiphasic biopolymer composite systems influence structure and properties.

Keywords: Polysaccharide thermomechanical processing; Chitosan; Carboxymethyl cellulose; Polyelectrolyte complexation; Graphene oxide; Glycerol

1 Introduction

In recent years, natural biopolymers such as cellulose, chitin/chitosan, starch, alginate and proteins (*e.g.* fibroin, collagen, and gelatin) have attracted huge interest in the development of materials for a wide range of applications from biomedical to pharmaceutical [1-6], in energy conversion and storage [7-10], electronic devices [11], for oil/water separation [12, 13], controlled fertiliser release [14, 15] and, for packaging and coatings [16-19]. The potential of biopolymers lies in their appealing properties and advantages over petro-derived polymers, such as renewability, wide availability, biodegradability, nontoxicity, and biocompatibility. Furthermore, these biological macromolecules have high versatility for chemical modification as they have multiple reactive sites (*e.g.* hydroxyl and amine groups) along their backbone chains. Moreover, some of these biopolymers display natural functionality such as the antimicrobial activity of chitosan.

To fabricate biopolymer materials with enhanced properties and functionality, material hybridisation has been an interesting approach. Relying on multiple dynamic bonds such as electrostatic interaction and hydrogen bonding between different components, biopolymer materials with engineered properties may be constructed [20, 21]. The concept of polyelectrolyte complexation (PEC) has been applied to create advanced biopolymer materials for various applications. For example, chitosan/alginate polyelectrolyte-complexed scaffolds showed both satisfactory cell adhesiveness [22] and mechanical properties [23]. Compared with chitosan alone, hydrogels based on PEC between chitosan and gelatin showed significantly improved 3D printability for fabricating high shape fidelity constructs with good biocompatibility for wound healing [24]. Chitosan/carboxymethyl cellulose (CMC) polyelectrolyte-complexed coatings displayed outstanding

barrier properties [25]. An underwater-implemented adhesive with exceptional strength was developed based on PEC between lignosulphonate and poly(amidoamine)-epichlorohydrin [26]. Our recent study [27] has revealed the unexpectedly higher hydrolytic stability of chitosan/CMC polyelectrolyte-complexed films compared with that of each biological component alone.

Another innovative approach to broaden the applicability of biopolymer materials is to hybridise biopolymers with nanomaterials [28-31]. Among different nanomaterials, graphene(s) have drawn the greatest attention due to their exceptional thermal conductivity, mechanical properties, and other electronic transport properties [32]. Moreover, graphenic nanomaterials have also demonstrated antimicrobial activity [33-36]. Hydrogels have been developed based on chitosan/graphene or chitosan/graphene oxide (GO) composites, showing excellent mechanical properties, electrical conductivity, tuneable swelling properties, biocompatibility, and antimicrobial activity [37, 38]. The excellent drug delivery behaviour of chitosan/GO composites have been demonstrated [39, 40]. Chitosan/graphene composites exhibited improved hydrothermal and chemical stability, allowing for the development of active packaging films, porous adsorbents for separation and metal removal, and stable catalytic supports in fine chemical synthesis [41].

In this work, different composite materials based on chitosan and chitosan/CMC polyelectrolyte-complexed matrices and GO/reduced GO (rGO) were prepared by thermomechanical processing. This "dry" method has been shown to be cost-effective for the processing and plasticisation of biopolymers [21, 27, 42-46], while in most reported studies, biopolymer/graphene composites were prepared by solution methods, which are solvent- and time-intensive. GO and rGO were used as functional fillers, which have different amounts of oxygen-containing groups (*e.g.*

─COOH and ─OH) and negative charges [47] and, thus, should display different degrees of hydrogen-bonding and electrostatic interactions with the biopolymers. In addition, we systematically investigated how glycerol, a cheap and most commonly used plasticiser for biopolymers, modified the structure and properties of these biopolymer/graphenic composites which, has not been reported widely before. Previous findings [31] have shown that polyols such as glycerol may negatively impact the dispersion of nanoclays or polysaccharide nanoparticles in plasticised starch materials; nonetheless, how these plasticisers will influence graphenic materials in biopolymer matrices remains largely unexplored. We hypothesise that in a polyelectrolyte-complexed biopolymer nanocomposite, the interactions between the biopolymers, plasticiser and nanofillers may counteract or complement each other depending on formulation. We elaborate on how these complex interactions in the multiphasic biopolymer composite systems influence their structure and properties, which could provide insights into the rational design of high-performance biopolymer materials for diverse applications.

2 Experimental

2.1 Materials

Chitosan (poly(β-(1,4)-D-glucosamine), derived from crab shells, with a weight-average molar mass (M_w) of about 150,000 g·mol^{-1}, a degree of deacetylation (DD) of >90%, and a viscosity of about 100 mPa·s (*i.e.* 1% solution in 1% acetic acid at 25 °C), was purchased from Shanghai Ryon Biological Technology Co., Ltd. (China). This chitosan was characterised previously [48]. CMC sodium, with a M_w of 90,000 g·mol^{-1}, a degree of substitution (DS) of 0.7, and a viscosity of 50–100 mPa·s (Brookfield, 2% solution, at 25 °C), was purchased from Shanghai Macklin Biochemical Co.,

Ltd. (China). The characteristics of this CMC are presented in our earlier report [27]. GO, in the form of an aqueous acid paste (25% GO, 74% water, and 1–1.5% HCl), was purchased from Abalonyx AS (Norway). Hydrazine hydrate solution (78–82% iodometric, Honeywell Fluka), ammonia solution (35%, AR, d = 0.88), and glycerol (≥99%, analytical grade) were supplied by Fisher Scientific UK Ltd., formic acid (98% w/w AR) and NaBr (pure) by Scientific Laboratory Supplies Ltd. (UK). Deionised water was used for all experiments. rGO was synthesised from GO with the detailed procedure described in our previous publication [49].

2.2 Sample preparation

Table 1 shows the formulations and codes of different samples prepared in this work. In these codes, the starting letter "A" denotes the matrix was chitosan alone while the letter "B" indicates chitosan/CMC was the matrix. The glycerol content is represented by the letter "G" and a suffix number, for example, "G2" is 20% glycerol. The last letter "F" signifies that the processed samples were films.

The samples were prepared following our previously-reported method [27]. Briefly, GO or rGO was dispersed in 25 mL of 2M formic acid solution by sonication using a tip-type sonicator (200 W, 24 kHz) for 10 min. Chitosan and/or CMC were pre-blended mechanically for 20 min, during which 2M formic acid solution (90 mL) and the treated nanoclay suspension (25 mL) were added dropwise. The liquid added during pre-blending could be fully absorbed by the biopolymers. The pre-blended mixtures were stored hermetically overnight in a fridge before thermomechanical mixing and compression moulding. The thermomechanical mixing was carried out using a HAAKE Rheomix OS Lab Mixer (Thermo Fisher Scientific, Waltham, MA, USA) at a rotor speed of 30 rpm and a

temperature of 80 °C for 15 min. The thermally-processed materials were compression-moulded into films of 150 mm × 150 mm × 1.2 mm using a COLLIN P200 P/M platen press (COLLIN Lab & Pilot Solutions GmbH, Ebersberg, Germany) at 110 °C and 160 bar for 10 min, followed by cooling to room temperature (RT) for another 5 min. The compression-moulded films were conditioned at 57% relative humidity (RH) for three weeks before characterisation. During conditioning, toluene was placed to prevent the samples from becoming mouldy. After conditioning, Type V dumbbell-shaped specimens were cut from the sheets according to ASTM Standard D638-14, which were then left openly at RT for two days before characterisation.

2.3 Sample characterisation

Scanning electron microscopy (SEM) imaging was performed using a ZEISS SIGMA field-emission scanning electron microscope with an acceleration voltage of 6 kV. The biopolymer films were cryo-fractured using liquid nitrogen and the samples sputter-coated with gold/palladium before imaging.

Scanning transmission electron microscopy (STEM) was conducted using a Talos F200X transmission electron microscope at 200 kV to obtain both bright-field (BF) and high-angle annular dark-field (HAADF) images. Ribbons about 60 nm thick were sectioned from epoxy-embedded sample blocks and subsequently transferred onto holey carbon films on 200-mesh copper grids. No liquid was used during preparation to avoid damaging the samples.

X-ray diffraction (XRD) analysis was undertaken using a PANalytical Empyrean X-ray diffractometer at 40 kV and 40 mA with a Co target (Kα = 1.790307Å) and a beam slit of 10 mm.

The samples were scanned over an angular range (2θ) of 6–40° with a step size of 0.0263° and a step rate of 2.16 s/step.

Fourier-transform infrared (FTIR) spectra were collected using a Bruker TENSOR 27 FTIR spectrometer with an attenuated total reflection (ATR) accessory with 32 scans for each sample over a range of 4000–500 cm^{-1} at room temperature (RT).

Thermo-gravimetric analysis (TGA) was undertaken using a Mettler Toledo TGA apparatus over a temperature range of 30–700 °C at 10 K/min under nitrogen.

Dynamic mechanical thermal analysis (DMTA) was performed using a Tritec 2000 DMA (Triton Technology Ltd., UK) in the dual cantilever mode with a sample length of 5 mm at a displacement of 0.01 mm. Temperature scans were performed from −100 °C to 180 °C at 2 °K/min and 1 Hz. The dynamic storage modulus (E'), loss modulus (E''), and loss tangent (tan $\delta = E''/E'$) were automatically calculated by the software.

Electrical impedance spectroscopy (EIS) was performed using a Princeton Applied Research PARSTAT MC (PMC) multi-channel potentiostat (Ametek Scientific Instruments, USA) with a PMC-2000 card and a two-point probe. The two surfaces of samples were painted with carbon conductive grease (No.8481, MG Chemicals, Canada) in designated areas (24 × 24 mm). At least triplicate tests were performed for each sample. The real (Z') and imaginary (Z'') parts of impedance were acquired with a frequency (f) range of $1–10^6$ Hz. The AC conductivity (admittance) (σ), the real part of relative permittivity (ε'_r), and the imaginary part of electric modulus (M'') calculated using the following equations [50-52]:

$$\sigma = \frac{Z\prime}{Z\prime^2 + Z\prime\prime^2} \cdot \frac{t}{A} \qquad (1)$$

$$\varepsilon'_r = \frac{-Z''}{Z'^2+Z''^2} \cdot \frac{t}{\omega A \varepsilon_0} \quad (2)$$

$$M'' = \frac{\varepsilon''}{\varepsilon'^2+\varepsilon''^2} \quad (3)$$

Here, ω is the angular frequency (= $2\pi f$), ε_0 is the permittivity of free space (≈ 8.854 ×10^{-12} F·m^{-1}), A is the area tested of the sample (m^2), and t is the sample thickness (m).

The bulk resistance (R_b) was determined from the Nyquist plots of impedance (Z'' *vs.* Z') from the points where the semicircle and the straight line meet. Then, the conductivity (σ_{dc}) was calculated using equation (4) [50, 53]:

$$\sigma_{dc} = \frac{t}{R_b \cdot A} \quad (4)$$

Tensile tests were performed using an Instron 3367 universal testing machine with a 1kN load cell at a crosshead speed of 3 mm/min. As the specimens were in the form of thin sheets, specimen extension was measured by grip separation as recommended by ASTM Standard D882. Young's modulus (E), tensile strength (σ_t), and elongation at break (ε_b) were automatically determined using Instron Bluehill 3 software from at least seven replicates for each sample.

Contact angle data were obtained from sessile tests at RT based on Young–Laplace using an Attension Theta Lite instrument (Biolin Scientific, UK). As the contact angle kept changing after the water drop was placed on the biopolymer film surface, contact angles at 0 s and 60 s (θ_{c0s} and θ_{c60s}, respectively) were recorded.

3 Results and Discussion

3.1 Morphology

According to the SEM images (**Figure S1**), the original chitosan and CMC have been successfully converted into cohesive, plasticised materials by thermomechanical processing. STEM

was used to examine the dispersion of GO or rGO in the biopolymers, see **Figure 1**. All the A-samples displayed some non-dispersed particulate features of different sizes up to 100 nm, as illustrated by the bright areas in HAADF images. This could represent some chitosan structures that were not disrupted by processing or new crystals evolved (discussed in XRD results). Compared with AG2-F, AG2/GO-F and AG2/rGO-F showed very similar morphology, except that there were some large-sized flocculent substances, some of which were over several hundreds of nanometres in length. They appeared as the 'cloudy' areas with diffused bright contrast in the HAADF image, indicative of a dissolvable feature which, may be ascribed to partially exfoliated GO or rGO nanosheets. In general, this observation indicates that, due to the matching chemistry and the thermomechanical mixing, both GO or rGO nanosheets were largely exfoliated and finely dispersed in the chitosan matrix. Likely, the resultant few-layer nanosheets at a certain small size became invisible under STEM against the background of the biopolymer matrix. In particular, GO nanosheets have oxygen-containing groups (*e.g.* ─COOH and ─OH) and negative charges resulting from the ionisation of carboxylic acid and phenolic hydroxyl groups, which can interact adequately with the polycationic chitosan through hydrogen bonding and electrostatic attraction [47]. In agreement with this, previous studies [47, 54, 55] have also demonstrated the excellent dispersion of GO in chitosan materials. Although rGO is less hydrophilic and contains less negatively charges than GO, the interactions between rGO and the chitosan matrix should be complemented by the sufficient mixing of the high-viscosity system during thermomechanical kneading, still resulting in notable dispersion of rGO nanosheets.

Compared with the A-series, the B-samples presented a clearer morphology. While most of the areas of BG2/GO-F and BG2/rGO-F were clear, some large floccules were visible, which are most likely agglomerated GO or rGO nanosheets. As these agglomerates were present in small number and scattered distantly (in the area examined), we consider in the B-composites, GO/rGO was still well dispersed. The greater level of agglomeration may be caused by PEC between the chitosan polycation and the CMC polyanion and, by the negative charges of CMC.

While previous studies [45, 56, 57] have indicated a possible phase separation between low- and high-glycerol-content domains in plasticised biopolymer composites, no such heterogeneity was observed in both the A- and B- samples here from SEM and STEM imaging, confirming the adequate mixing of the materials.

3.2 Crystalline structure

The crystalline structures of the different biopolymer and composite films were revealed by XRD, see diffractograms in **Figure 2**. As shown in **Figure 2** (a), all the A-samples displayed similar XRD patterns. The reflections are all attributed to the crystal lattice of chitosan [58]. As discussed earlier [27], the crystalline patterns shown here are largely different from those of unprocessed chitosan and, therefore, are in the main due to processing-induced re-crystallisation. Clearly, AG4-F displayed weaker peak intensities than the A-samples with 20 wt% glycerol, indicating a greater amount of glycerol can hinder the re-crystallisation of chitosan. However, AG4/GO-F, and AG4/rGO-F displayed XRD patterns with increased peak intensities, suggesting the addition of GO/rGO might assist the re-crystallisation of the plasticised chitosan. The electrostatic interaction

and hydrogen bonding may facilitate the arrangement of the attached chitosan chains to form an ordered structure along the rigid template offered by GO [47].

Figure 2 (b) shows that all the B-samples were mainly amorphous. The processing has eliminated the majority of the original crystalline structure of the biopolymers. The addition of CMC to the matrix effectively suppressed re-crystallisation of chitosan, due to the strong hydrogen-bonding and electrostatic interactions between the two negatively-charged polysaccharides. The content of glycerol or the addition of GO or rGO did not vary the amorphous nature of this dual-biopolymer system.

3.3 Molecular interactions

Figure 3 presents the FTIR spectra for the different films. As shown in **Figure 3** (a), the six A-samples displayed very similar FTIR patterns. Plasticisation by 20 wt% only cause a slight blue shift of the absorption band originally at 1022 cm^{-1}. With a higher glycerol content (40 wt%) as plasticiser, both the absorption bands at 1572 cm^{-1} (indicative of the N─H bending from amine and amide II) and at 1022 cm^{-1} (skeletal vibration of C─O stretching) [59-61] were blue shifted. Inclusion of glycerol resulted in changes in the hydrogen-bonding interactions involving the amino (─NH_2) and amide (containing ─NH─) groups of chitosan (not 100% deacetylated) and made the chitosan chains more mobile (in agreement with there being reduced crystallinity).

It can be seen from **Figure 3** (b) that the six B-samples displayed FTIR spectra similar to those for the A-series. The more pronounced peak at 1414 cm^{-1} can be attributed to the asymmetric stretching vibration of the carboxylate ions of CMC. The characteristic bands for CMC at 1055 cm^{-1} (C─O stretching vibration of ether groups) and 1589 cm^{-1} (symmetric stretching vibration of

carboxylate ions) [62-65] might be overlapped by the chitosan signals. Compared with the A-samples, a greater blue shift in the band position at 1572 cm^{-1} can be seen suggesting strong interactions between chitosan and CMC via the amino or amide groups. Moreover, compared with the A-samples containing 20 wt% glycerol, BG2-F, BG2/GO-F, BG2/rGO-F showed a slight blue shift in position of the peak originally at 1022 cm^{-1}, and this band was more apparently blue-shifted for BG4-F, BG4/GO-F, and BG4/rGO-F. Thus, the plasticisation by glycerol increased the mobility of chitosan chains.

Irrespective of matrix type, the addition of either GO or rGO is not observed to cause apparent changes in the FTIR spectrum. Likely, the interactions involving GO and rGO are not visible in the FTIR spectra due to their low content in the matrices, but they are also not very IR-active materials.

3.4 Thermal stability

Figure 4 shows the TGA data for the different films presented as the derivative of weight loss as a function of temperature. For AG2-F, the major thermal decomposition of chitosan occurred between 215 °C and 385 °C, with its peak temperature (T_d, when the weight loss occurs at the maximum rate) being 286 °C. Immediately before this major weight loss, there was a small peak between 195 °C and 215 °C, associated with the initial de-polymerisation of the biopolymer. Compared with AG2-F, AG2/GO-F and AG2/rGO-F exhibited slightly lower T_d (284 °C and 281 °C, respectively). The GO used in this study is relatively thermally unstable with the major mass loss occurring between about 150 and 240 °C peaked at 207 °C [49], presumably due to pyrolysis of the labile oxygen-containing functional groups, whereas rGO is more thermally stable [66]. The thermal decomposition of glycerol starts as early as 155 °C and concludes at 237 °C [67], which is also more

thermally sensitive than chitosan. The thermal decomposition of GO and glycerol in an early stage could create radicals, which accelerated the thermal decomposition of chitosan. Considering the T_d value of the processed chitosan without plasticiser (A-F) being 297 °C [27], it is proposed that glycerol had a greater effect than GO in reducing the thermal stability of chitosan. Glycerol could weaken the hydrogen-bonding network of chitosan, further leading to reduced thermal stability. Regarding the reduced T_d of AG2/rGO-F, the inclusion of rGO in the system might have weakened the hydrogen-bonding interactions between the chitosan chains in addition to the effect glycerol played.

AG4-F exhibited a T_d value of 263 °C, significantly lower than that of the three A-samples with a lower glycerol content. Again, this shows the strong effect of glycerol in reducing the thermal stability of chitosan. Compared with AG4-F, AG4/rGO displayed a very similar T_d value (264 °C) whereas the T_d of AG4/GO-F increased to 277 °C. The enhanced thermal stability of AG4/GO-F might be derived from the increased crystallinity (see XRD results) resulting from the addition of GO.

Figure 4 (b) reveals that all the B-samples, regardless of glycerol content or GO/rGO addition, had very similar T_d values (about 269 °C). Adjacent to the major peak, there was an overlapped peak at a higher temperature (318–320 °C), even higher than the T_d of the processed chitosan without plasticiser (A-F) (297 °C) [27]. This small peak may be due to the biopolymer polyelectrolyte complexes inducing enhanced thermal stability. The T_d values of all the B-samples plasticised with glycerol are significantly lower than that of the thermomechanically-processed chitosan/CMC film without plasticiser (B-F) (273 °C) [27]. This, again, suggests the inclusion of glycerol decreases the

thermal stability of the biopolymers. Also, the T_d values of the B-samples with 20 wt% glycerol was lower than those of the A-samples with the same glycerol content, suggesting inclusion of CMC leads to a reduction in the thermal stability of the whole biopolymer matrix. However, the T_d values of all the B-samples were remarkably higher than those of the A-samples with 40 wt% glycerol, strongly implying that PEC between chitosan and CMC had counteracted the effect of glycerol on thermal stability.

3.5 Molecular relaxations

DMTA was used to study the molecular relaxation of the different films, with tan δ plots as a function of temperature shown in **Figure 5**. For all the samples, two transitions could be identified. A weak one occurring at sub-zero temperatures is associated with a β-relaxation of chitosan attributed to the side chain or lateral group motions of chitosan interacting with small molecules such as water or glycerol by hydrogen bonding. At higher temperatures, there was a much more prominent transition attributed to the α-transition (glass transition) of chitosan [68, 69]. For AG2-F, the peak temperature of the β-transition (T_β) was −40 °C and the peak temperature of the α-transition (T_α) was at 54 °C. AG/rGO-F showed unchanged relaxation peak temperatures whereas AG/GO-F displayed increased T_α and T_β values (−37 °C and 61 °C). Clearly, the hydrogen-bonding and electrostatic interactions between GO and chitosan restrict chain movement of the glycerol-plasticised chitosan.

Compared with the A-samples with 20 wt% glycerol, AG4-F, AG4/GO-F and AG4/rGO-F displayed reduced relaxation peak temperatures. For AG4-F, T_β was −46 °C and T_α was 31 °C. At this glycerol level, the addition of GO, again, increased both T_β and T_α, whilst rGO was ineffective at

changing these transition temperatures. This result demonstrates the strong affinity between chitosan and GO even with a high glycerol content in the system.

With the same amount (20 wt%) of glycerol, the B-samples exhibited distinctly increased T_β and T_α than the A samples, suggesting decreased biopolymer chain mobility induced by PEC. Specifically, the values of T_β and T_α for BG2-F was −37 °C and 87 °C, respectively. In comparison, BG2/GO-F and BG2/rGO-F had slightly reduced T_α (81 °C and 84 °C, respectively) while T_β was unchanged. In this regard, the addition of GO or rGO may have disrupted PEC and hydrogen bonding between the two biopolymers, with GO being more effective. That is, the addition of GO or rGO to the polyelectrolyte-complexed matrix promoted biopolymer chain movement instead of restricting it.

Compared with the B-samples with 20 wt% glycerol, a higher content of glycerol clearly led to decreased T_β and T_α. Specifically, BG4-F had T_β = −44 °C and T_α = 67 °C, which were not changed with the addition of either GO or rGO (*i.e.* for BG4/GO-F and BG4/rGO-F). In this case, the effect of GO or rGO on biopolymer chain mobility may be negligible because of the high glycerol content plasticising the biopolymers.

3.6 Electrochemical properties

Figure 6 (a) and (b) show the Nyquist plots consisting of a half semicircle at *f* characteristic of a combination of bulk resistance and bulk capacitance in parallel [70]. The bigger the semicircular, the larger is the bulk resistance. Based on these plots, the calculated R_b and σ_{dc} [70] are listed in **Table S1**. The A-samples with 20 wt% glycerol irrespective of nanofiller type had σ_{dc} values similar to that of A-F [27]. Increasing the glycerol content to 40 wt% led to significantly higher σ_{dc}, while at this

glycerol level, the effect of GO or rGO addition was minor. In this regard, the plasticiser increased the mobility of electrical charges (ions and dipoles) in the biopolymer composite system. While the σ_{dc} values of BG2-F and BG2/rGO-F were similar to that of AG2-F, BG2/GO-F had a lower σ_{dc}. Possibly, the interactions of GO with the biopolymers and glycerol reduced the mobility of electrical charges in the system. The B-samples with 40 wt% glycerol displayed higher σ_{dc}, whereas the effect of GO or rGO was insignificant.

Figure 6 (c) and (d) show that σ increased with f, which is typical of an insulating material (dielectric). The value of σ at low f can be attributed to the accumulation of charged species at the electrode–electrolyte interface; hence, there are less mobile ions in the bulk material to contribute towards conductivity [50]. It can be noted that the samples with rGO added had a much higher σ at low f and reduced f-dependence of σ.

Figure 6 (e) and (f) show that for all the samples, decreasing f led to an abrupt increase in ε'_r. The high ε'_r values at low f indicate electrode polarisation and space charge effects (dipole moment) [71, 72]. Among the different samples, those containing rGO exhibited the highest ε'_r at low f. In this regard, rGO assists the accumulation of mobile ions. Moreover, all the samples had impressively high ε'_r as listed in **Table S1**. BG2/GO-F and BG2/rGO-F had the lowest ε'_r values at 1 kHz, 56±3 and 54±14, respectively. AG4-F had the highest ε'_r at 1 kHz, 387±110, followed by BG4/GO-F whose ε'_r at 1 kHz was 307±72. Thus, these biopolymer materials have potential for use in some electronic applications such as energy storage.

Figure 6 (g) and (h) show that at high f, M'' exhibited a well-defined peak, indicating relaxation processes with distributed relaxation times (*i.e.* viscoelastic relaxation, or dipolar relaxation) [53].

For both matrices, increasing the glycerol content from 20 wt% to 40 wt% shifted the peak position to a higher *f*, suggesting a decreased relaxation time. Obviously, more plasticiser in the system could increase polymer chain mobility and thus, make ions and associated dipoles more mobile. The influence of GO or rGO inclusion on the relaxation process was minor.

3.7 Mechanical properties

Figure 7 (a) and (b) show representative stress–strain curves for the different films under tensile testing. The A-samples with 40 wt% glycerol content behave more like elastomeric materials whereas the stress-strain curves for the other samples were typical of a hard and tough plastic with strain hardening. Based on these curves, the calculated E, σ_t, and ε_b are plotted in **Figure 7** (c), (d) and (e), respectively. Overall, all these mechanical properties are influenced by glycerol content and GO or rGO addition. Regardless of matrix, a higher glycerol content generally caused reductions in E and σ_t and an increase in ε_b (except for AG4-F). Glycerol could restrict hydrogen bonding and act as spacers between biopolymer chains, making the material more ductile.

For the A-matrix with 20 wt% glycerol, the addition of GO resulted in a moderate increase in E with unchanged σ_t, whereas rGO showed a negative effect on both E and σ_t. This was likely to be a consequence of the weaker molecular interactions with the presence of rGO and glycerol. For the B-matrix with 20 wt% glycerol, inclusion of GO or rGO led to a reduction in E and σ_t, which could be due to the diminished PEC and interactions between the two biopolymers with GO or rGO.

For the samples with inclusion of 40 wt% glycerol, some positive effects of GO or rGO on mechanical properties could be seen. For example, the σ_t values of AG4/GO-F and AG4/rGO-F were 13.4±1.1 MPa and 11.6±1.0 MPa, respectively, higher than that of AG4-F (8.5±0.5 MPa).

Interestingly, AG4/GO-F and AG4/rGO-F displayed significantly higher ε_b values (99.8±10.7% and 98.9±9.7%) than that of AG4-F (58.8±5.1%). This result demonstrates the increased toughness of the 40-wt%-glycerol-plasticised chitosan film with the addition of GO or rGO. In this regard, the interactions between the chitosan chains and the finely dispersed GO/rGO platelets may not only counteract the plasticisation effect of glycerol and assist re-crystallisation (see XRD results), but also facilitate uniform stress distribution and minimise stress concentration, leading to increased mechanical properties [47, 55]. However, this mechanical reinforcement effect was not apparent for the B-samples with 40 wt% glycerol, due to the less effective interactions between GO or rGO and biopolymer chains in the polyelectrolyte-complexed system.

The Shore D hardness of the different samples was measured as shown in **Figure S2**, which correspond well with the trends obtained for E and σ_t data. This means glycerol plasticisation and the addition of GO or rGO affected the surface rigidity in the same way as for the tensile properties.

3.8 Surface wettability

The surface wettability of the different films is reflected by θ_{c0s} and θ_{c60s} as shown in **Figure 8**. AG2-F displayed θ_{c0s} = 80±7° and θ_{c60s} = 49±7°, lower than the relative values for A-F (θ_{c0s} = 90±5° and θ_{c60s} = 68±5°) [27], indicating that plasticisation of chitosan with 20 wt% glycerol resulted in increased surface hydrophilicity of the chitosan film, which could be attributed to the hygroscopicity (the water binding capacity) of the plasticiser [73]. AG2/GO-F had unchanged θ_{c0s} and θ_{c60s} values to those of AG2-F, suggesting the addition of GO nanosheets did not vary the surface hydrophilicity of the 20-wt%-glycerol-plasticised chitosan. Addition of rGO, which is more hydrophobic than GO,

AG2/rGO-F showed slightly reduced surface hydrophilicity (θ_{c0s} = 85±5° and θ_{c60s} = 61±3°), *i.e.* slightly more hydrophobic.

Interestingly, AG4-F had a θ_{c0s} value slightly higher than that of AG2-F while its θ_{c60s} was similar to that of AG2-F. It may be that for a higher glycerol content there is more interaction with chitosan chains resulting in less free chitosan hydroxyl groups available, resulting in reduced surface hydrophilicity initially, while over time testing would allow water molecules to interact with the hydroxyls of chitosan and glycerol. Compared with AG4-F, AG4/GO-F showed slightly increased surface hydrophilicity while AG4/rGO-F displayed a slight reverse change, which could be due to the higher hydrophobicity of rGO.

While our previous work [27] showed that B-F had increased surface hydrophilicity (θ_{c0s} = 71±6° and θ_{c60s} = 60±5°) more than A-F, here, BG2-F had clearly higher θ_{c0s} (90±6°) and θ_{c60s} (73±8°) than AG2-F. This suggests that glycerol plasticisation increased the surface hydrophobicity of the dual-biopolymer system, derived from the enhanced chain mobility and, thus, PEC by glycerol. However, when either GO or GO was added or a higher glycerol content (40 wt%) was used, the B-samples had significantly increased surface hydrophilicity. This would suggest that the interactions between the two biopolymers were interrupted by addition of GO or rGO or excess glycerol.

In summary, the contact angle results show that for chitosan, the greater the glycerol content, the more the surface hydrophilicity was reduced, and addition of rGO could reduce this effect further. When the polyelectrolyte-complexed biopolymer (B) matrix was used, plasticisation with 20 wt%

glycerol without the addition of GO or rGO gave the most hydrophobic surface, better than that of all the A samples.

4 Conclusions

In this study, different glycerol-plasticised biopolymer composites were successfully prepared by thermomechanical processing. In all these samples, the excellent dispersion of GO or rGO was confirmed by STEM. However, glycerol content and the matrix type (single- or dual-biopolymer) played the dominant role in determining material structure and properties. Specifically, inclusion of glycerol weakened interactions between chitosan chains, enhancing chain mobility, resulting in reduced crystallinity, thermal stability and mechanical properties. This plasticiser could also increase the mobility of ions and dipoles in the system and thus, vary electrical conductivity. In contrast, PEC with CMC restricted chitosan chain mobility and suppress crystallinity. Interestingly, glycerol may assist PEC by increasing biopolymer chain mobility, leading to reduced surface hydrophilicity.

GO or rGO interacted with chitosan chains, leading to changes in biopolymer structure and properties under certain conditions. For the A-matrix, addition of GO or rGO to chitosan could enhance crystallinity, decrease chain mobility and thereby, contribute to increased mechanical properties. For the B-matrix, GO and rGO interfered with PEC, resulting in decreased mechanical properties and increased surface hydrophilicity. While GO has a strong affinity with chitosan, rGO, being more electrically conductive, was more effective at increasing the AC conductivity of the composites at low *f*. Besides, rGO reduced the surface hydrophilicity of the biopolymers as disrupted the biopolymer chain interactions. The effects of GO or rGO on PEC and hydrogen bonding interactions between biopolymer chains were illustrated in **Figure 9**.

This study has revealed the complex phase interactions within plasticised, polyelectrolyte-complexed biopolymer composites. The holistic understanding of such multiphase systems can provide new insights into the rational design of biopolymer composite materials with tailored properties.

Conflicts of Interests

Declarations of interest: none

Acknowledgements

The authors acknowledge funding from the European Union's Horizon 2020 research and innovation programme under the Marie Skłodowska-Curie grant agreement No. 798225. P. Chen acknowledges the financial support from the China Scholarship Council (CSC) for her visiting position and thanks IINM, WMG, University of Warwick, UK for hosting her research visit. F. Xie also acknowledges support from the Guangxi Key Laboratory for Polysaccharide Materials and Modification, Guangxi University for Nationalities, China (Grant No. GXPSMM18ZD-02).

References

[1] W. Xu, X. Wang, N. Sandler, S. Willför, C. Xu, Three-Dimensional Printing of Wood-Derived Biopolymers: A Review Focused on Biomedical Applications, ACS Sustainable Chem. Eng. 6(5) (2018) 5663-5680.

[2] J. Chen, F. Xie, X. Li, L. Chen, Ionic liquids for the preparation of biopolymer materials for drug/gene delivery: a review, Green Chem. 20(18) (2018) 4169-4200.

[3] S.-B. Park, E. Lih, K.-S. Park, Y.K. Joung, D.K. Han, Biopolymer-based functional composites for medical applications, Prog. Polym. Sci. 68 (2017) 77-105.

[4] S. Van Vlierberghe, P. Dubruel, E. Schacht, Biopolymer-Based Hydrogels As Scaffolds for Tissue Engineering Applications: A Review, Biomacromolecules 12(5) (2011) 1387-1408.

[5] A. Lee, A.R. Hudson, D.J. Shiwarski, J.W. Tashman, T.J. Hinton, S. Yerneni, J.M. Bliley, P.G. Campbell, A.W. Feinberg, 3D bioprinting of collagen to rebuild components of the human heart, Science 365(6452) (2019) 482-487.

[6] X. Lin, Y. Liu, A. Bai, H. Cai, Y. Bai, W. Jiang, H. Yang, X. Wang, L. Yang, N. Sun, H. Gao, A viscoelastic adhesive epicardial patch for treating myocardial infarction, Nat. Biomed. Eng. 3(8) (2019) 632-643.

[7] J. Ma, Y. Sahai, Chitosan biopolymer for fuel cell applications, Carbohydr. Polym. 92(2) (2013) 955-975.

[8] R. Wang, S. Gao, Z. Yang, Y. Li, W. Chen, B. Wu, W. Wu, Engineered and Laser‐Processed Chitosan Biopolymers for Sustainable and Biodegradable Triboelectric Power Generation, Adv. Mater. 30(11) (2018) 1706267.

[9] J. Wan, J. Zhang, J. Yu, J. Zhang, Cellulose Aerogel Membranes with a Tunable Nanoporous Network as a Matrix of Gel Polymer Electrolytes for Safer Lithium-Ion Batteries, ACS Appl. Mater. Interfaces 9(29) (2017) 24591-24599.

[10] Q. Zheng, A. Kvit, Z. Cai, Z. Ma, S. Gong, A freestanding cellulose nanofibril-reduced graphene oxide-molybdenum oxynitride aerogel film electrode for all-solid-state supercapacitors with ultrahigh energy density, J. Mater. Chem. A (2017).

[11] J. Hou, M. Liu, H. Zhang, Y. Song, X. Jiang, A. Yu, L. Jiang, B. Su, Healable green hydrogen bonded networks for circuit repair, wearable sensor and flexible electronic devices, J. Mater. Chem. A (2017).

[12] J.J. Koh, G.J.H. Lim, X. Zhou, X. Zhang, J. Ding, C. He, 3D-Printed Anti-Fouling Cellulose Mesh for Highly Efficient Oil/Water Separation Applications, ACS Appl. Mater. Interfaces 11(14) (2019) 13787-13795.

[13] S. Zhang, F. Lu, L. Tao, N. Liu, C. Gao, L. Feng, Y. Wei, Bio-inspired anti-oil-fouling chitosan-coated mesh for oil/water separation suitable for broad ph range and hyper-saline environments, ACS Appl. Mater. Interfaces 5(22) (2013) 11971-11976.

[14] Y. Xiang, G. Zhang, Y. Chi, D. Cai, Z. Wu, Fabrication of a controllable nanopesticide system with magnetic collectability, Chem. Eng. J. 328(Supplement C) (2017) 320-330.

[15] X. Xiao, L. Yu, F. Xie, X. Bao, H. Liu, Z. Ji, L. Chen, One-step method to prepare starch-based superabsorbent polymer for slow release of fertilizer, Chem. Eng. J. 309 (2017) 607-616.

[16] D.S. Cha, M.S. Chinnan, Biopolymer-based antimicrobial packaging: A review, Critical Reviews in Food Science and Nutrition 44(4) (2004) 223-237.

[17] G. Cado, R. Aslam, L. Séon, T. Garnier, R. Fabre, A. Parat, A. Chassepot, J.C. Voegel, B. Senger, F. Schneider, Y. Frère, L. Jierry, P. Schaaf, H. Kerdjoudj, M.H. Metz-Boutigue, F. Boulmedais, Self-Defensive Biomaterial Coating Against Bacteria and Yeasts: Polysaccharide Multilayer Film with Embedded Antimicrobial Peptide, Adv. Funct. Mater. 23(38) (2013) 4801-4809.

[18] M.G.A. Vieira, M.A. da Silva, L.O. dos Santos, M.M. Beppu, Natural-based plasticizers and biopolymer films: A review, Eur. Polym. J. 47(3) (2011) 254-263.

[19] P. Bie, P. Liu, L. Yu, X. Li, L. Chen, F. Xie, The properties of antimicrobial films derived from poly(lactic acid)/starch/chitosan blended matrix, Carbohydr. Polym. 98(1) (2013) 959-966.

[20] Z. Jiang, A. Bhaskaran, H.M. Aitken, I.C.G. Shackleford, L.A. Connal, Using Synergistic Multiple Dynamic Bonds to Construct Polymers with Engineered Properties, Macromol. Rapid Commun. 40(10) (2019) 1900038.

[21] L. Meng, F. Xie, B. Zhang, D.K. Wang, L. Yu, Natural Biopolymer Alloys with Superior Mechanical Properties, ACS Sustainable Chem. Eng. 7(2) (2019) 2792-2802.

[22] N. Iwasaki, S.-T. Yamane, T. Majima, Y. Kasahara, A. Minami, K. Harada, S. Nonaka, N. Maekawa, H. Tamura, S. Tokura, M. Shiono, K. Monde, S.-I. Nishimura, Feasibility of Polysaccharide Hybrid Materials for Scaffolds in Cartilage Tissue Engineering: Evaluation of Chondrocyte Adhesion to Polyion Complex Fibers Prepared from Alginate and Chitosan, Biomacromolecules 5(3) (2004) 828-833.

[23] Z. Li, H.R. Ramay, K.D. Hauch, D. Xiao, M. Zhang, Chitosan–alginate hybrid scaffolds for bone tissue engineering, Biomaterials 26(18) (2005) 3919-3928.

[24] W.L. Ng, W.Y. Yeong, M.W. Naing, Polyelectrolyte gelatin-chitosan hydrogel optimized for 3D bioprinting in skin tissue engineering, Int. J. Bioprint. 2(1) (2016) 10.

[25] S. Basu, A. Plucinski, J.M. Catchmark, Sustainable barrier materials based on polysaccharide polyelectrolyte complexes, Green Chem. 19(17) (2017) 4080-4092.

[26] C. Wei, X. Zhu, H. Peng, J. Chen, F. Zhang, Q. Zhao, Facile Preparation of Lignin-Based Underwater Adhesives with Improved Performances, ACS Sustainable Chem. Eng. 7(4) (2019) 4508-4514.

[27] P. Chen, F. Xie, F. Tang, T. McNally, Thermomechanical-induced polyelectrolyte complexation between chitosan and carboxymethyl cellulose enabling unexpected hydrolytic stability, Compos. Sci. Technol. 189 (2020) 108031.

[28] M.M. Reddy, S. Vivekanandhan, M. Misra, S.K. Bhatia, A.K. Mohanty, Biobased plastics and bionanocomposites: Current status and future opportunities, Prog. Polym. Sci. 38(10–11) (2013) 1653-1689.

[29] R. Xiong, A.M. Grant, R. Ma, S. Zhang, V.V. Tsukruk, Naturally-derived biopolymer nanocomposites: Interfacial design, properties and emerging applications, Mater. Sci. Eng., R 125 (2018) 1-41.

[30] F. Chivrac, E. Pollet, L. Avérous, Progress in nano-biocomposites based on polysaccharides and nanoclays, Mater. Sci. Eng., R 67(1) (2009) 1-17.

[31] F. Xie, E. Pollet, P.J. Halley, L. Avérous, Starch-based nano-biocomposites, Prog. Polym. Sci. 38(10-11) (2013) 1590-1628.

[32] T. Kuilla, S. Bhadra, D. Yao, N.H. Kim, S. Bose, J.H. Lee, Recent advances in graphene based polymer composites, Prog. Polym. Sci. 35(11) (2010) 1350-1375.

[33] J. Chen, H. Peng, X. Wang, F. Shao, Z. Yuan, H. Han, Graphene oxide exhibits broad-spectrum antimicrobial activity against bacterial phytopathogens and fungal conidia by intertwining and membrane perturbation, Nanoscale 6(3) (2014) 1879-1889.

[34] F. Perreault, A.F. de Faria, S. Nejati, M. Elimelech, Antimicrobial Properties of Graphene Oxide Nanosheets: Why Size Matters, ACS Nano 9(7) (2015) 7226-7236.

[35] M. Di Giulio, R. Zappacosta, S. Di Lodovico, E. Di Campli, G. Siani, A. Fontana, L. Cellini, Antimicrobial and Antibiofilm Efficacy of Graphene Oxide against Chronic Wound Microorganisms, Antimicrob. Agents Chemother. 62(7) (2018) e00547-18.

[36] A. Al-Jumaili, S. Alancherry, K. Bazaka, M.V. Jacob, Review on the Antimicrobial Properties of Carbon Nanostructures, Materials 10(9) (2017) 1066.

[37] S. Sayyar, E. Murray, B.C. Thompson, J. Chung, D.L. Officer, S. Gambhir, G.M. Spinks, G.G. Wallace, Processable conducting graphene/chitosan hydrogels for tissue engineering, J. Mater. Chem. A 3(3) (2015) 481-490.

[38] A. Konwar, S. Kalita, J. Kotoky, D. Chowdhury, Chitosan–Iron Oxide Coated Graphene Oxide Nanocomposite Hydrogel: A Robust and Soft Antimicrobial Biofilm, ACS Appl. Mater. Interfaces 8(32) (2016) 20625-20634.

[39] R. Justin, B. Chen, Characterisation and drug release performance of biodegradable chitosan–graphene oxide nanocomposites, Carbohydr. Polym. 103 (2014) 70-80.

[40] R. Wang, D. Shou, O. Lv, Y. Kong, L. Deng, J. Shen, pH-Controlled drug delivery with hybrid aerogel of chitosan, carboxymethyl cellulose and graphene oxide as the carrier, Int. J. Biol. Macromol. 103 (2017) 248-253.

[41] S. Frindy, A. Primo, H. Ennajih, A. el kacem Qaiss, R. Bouhfid, M. Lahcini, E.M. Essassi, H. Garcia, A. El Kadib, Chitosan–graphene oxide films and CO2-dried porous aerogel microspheres: Interfacial interplay and stability, Carbohydr. Polym. 167 (2017) 297-305.

[42] V. Epure, M. Griffon, E. Pollet, L. Avérous, Structure and properties of glycerol-plasticized chitosan obtained by mechanical kneading, Carbohydr. Polym. 83(2) (2011) 947-952.

[43] D.F. Xie, V.P. Martino, P. Sangwan, C. Way, G.A. Cash, E. Pollet, K.M. Dean, P.J. Halley, L. Avérous, Elaboration and properties of plasticised chitosan-based exfoliated nano-biocomposites, Polymer 54(14) (2013) 3654-3662.

[44] C. Gao, E. Pollet, L. Avérous, Properties of glycerol-plasticized alginate films obtained by thermo-mechanical mixing, Food Hydrocolloids 63 (2017) 414-420.

[45] F. Chivrac, E. Pollet, M. Schmutz, L. Avérous, New approach to elaborate exfoliated starch-based nanobiocomposites, Biomacromolecules 9(3) (2008) 896-900.

[46] P. Chen, F. Xie, F. Tang, T. McNally, Unexpected plasticization effects on the structure and properties of polyelectrolyte complexed chitosan/alginate materials, ACS Applied Polymer Materials xxx(xxx) (2020) xxx-xxx (DOI: 10.1021/acsapm.0c00433).

[47] X. Yang, Y. Tu, L. Li, S. Shang, X.-m. Tao, Well-Dispersed Chitosan/Graphene Oxide Nanocomposites, ACS Appl. Mater. Interfaces 2(6) (2010) 1707-1713.

[48] P. Chen, F. Xie, F. Tang, T. McNally, Structure and properties of thermomechanically processed silk peptide and nanoclay filled chitosan, Journal Polymer Science (2019) Submitted.

[49] P. Chen, F. Xie, F. Tang, T. McNally, Structure and properties of thermomechanically processed chitosan/carboxymethyl cellulose/graphene oxide polyelectrolyte complexed bionanocomposites, Int. J. Biol. Macromol. 158 (2020) 420-429.

[50] Z. Osman, Z.A. Ibrahim, A.K. Arof, Conductivity enhancement due to ion dissociation in plasticized chitosan based polymer electrolytes, Carbohydr. Polym. 44(2) (2001) 167-173.

[51] A.S. Bhatt, D.K. Bhat, M.S. Santosh, C.-w. Tai, Chitosan/NiO nanocomposites: a potential new dielectric material, J. Mater. Chem. 21(35) (2011) 13490-13497.

[52] R. Bowen Chris, S. Buschhorn, V. Adamaki, Manufacture and characterization of conductor-insulator composites based on carbon nanotubes and thermally reduced graphene oxide, Pure Appl. Chem. 86(5) (2014) 765-774.

[53] I.A. Fadzallah, S.R. Majid, M.A. Careem, A.K. Arof, Relaxation process in chitosan–oxalic acid solid polymer electrolytes, Ionics 20(7) (2014) 969-975.

[54] D. Han, L. Yan, W. Chen, W. Li, Preparation of chitosan/graphene oxide composite film with enhanced mechanical strength in the wet state, Carbohydr. Polym. 83(2) (2011) 653-658.

[55] Y. Pan, T. Wu, H. Bao, L. Li, Green fabrication of chitosan films reinforced with parallel aligned graphene oxide, Carbohydr. Polym. 83(4) (2011) 1908-1915.

[56] F. Chivrac, E. Pollet, M. Schmutz, L. Avérous, Starch nano-biocomposites based on needle-like sepiolite clays, Carbohydr. Polym. 80(1) (2010) 145-153.

[57] F. Chivrac, E. Pollet, P. Dole, L. Avérous, Starch-based nano-biocomposites: plasticizer impact on the montmorillonite exfoliation process, Carbohydr. Polym. 79(4) (2010) 941-947.

[58] F.S. Kittur, A.B. Vishu Kumar, R.N. Tharanathan, Low molecular weight chitosans—preparation by depolymerization with *Aspergillus niger* pectinase, and characterization, Carbohydr. Res. 338(12) (2003) 1283-1290.

[59] G. Lawrie, I. Keen, B. Drew, A. Chandler-Temple, L. Rintoul, P. Fredericks, L. Grøndahl, Interactions between Alginate and Chitosan Biopolymers Characterized Using FTIR and XPS, Biomacromolecules 8(8) (2007) 2533-2541.

[60] A. Pawlak, M. Mucha, Thermogravimetric and FTIR studies of chitosan blends, Thermochim. Acta 396(1-2) (2003) 153-166.

[61] Z. Chen, X. Mo, C. He, H. Wang, Intermolecular interactions in electrospun collagen–chitosan complex nanofibers, Carbohydr. Polym. 72(3) (2008) 410-418.

[62] R.K. Layek, A. Kundu, A.K. Nandi, High-Performance Nanocomposites of Sodium Carboxymethylcellulose and Graphene Oxide, Macromol. Mater. Eng. 298(11) (2013) 1166-1175.

[63] K. Shahzadi, I. Mohsin, L. Wu, X. Ge, Y. Jiang, H. Li, X. Mu, Bio-Based Artificial Nacre with Excellent Mechanical and Barrier Properties Realized by a Facile In Situ Reduction and Cross-Linking Reaction, ACS Nano 11(1) (2017) 325-334.

[64] N. El Miri, K. Abdelouahdi, A. Barakat, M. Zahouily, A. Fihri, A. Solhy, M. El Achaby, Bio-nanocomposite films reinforced with cellulose nanocrystals: Rheology of film-forming solutions, transparency, water vapor barrier and tensile properties of films, Carbohydr. Polym. 129(0) (2015) 156-167.

[65] C. Rosca, M.I. Popa, G. Lisa, G.C. Chitanu, Interaction of chitosan with natural or synthetic anionic polyelectrolytes. 1. The chitosan–carboxymethylcellulose complex, Carbohydr. Polym. 62(1) (2005) 35-41.

[66] S. Stankovich, D.A. Dikin, R.D. Piner, K.A. Kohlhaas, A. Kleinhammes, Y. Jia, Y. Wu, S.T. Nguyen, R.S. Ruoff, Synthesis of graphene-based nanosheets via chemical reduction of exfoliated graphite oxide, Carbon 45(7) (2007) 1558-1565.

[67] B. Dou, V. Dupont, P.T. Williams, H. Chen, Y. Ding, Thermogravimetric kinetics of crude glycerol, Bioresour. Technol. 100(9) (2009) 2613-2620.

[68] I. Quijada-Garrido, B. Laterza, J.M. Mazón-Arechederra, J.M. Barrales-Rienda, Characteristic Features of Chitosan/Glycerol Blends Dynamics, Macromol. Chem. Phys. 207(19) (2006) 1742-1751.

[69] I. Quijada-Garrido, V. Iglesias-González, J.M. Mazón-Arechederra, J.M. Barrales-Rienda, The role played by the interactions of small molecules with chitosan and their transition temperatures. Glass-forming liquids: 1,2,3-Propantriol (glycerol), Carbohydr. Polym. 68(1) (2007) 173-186.

[70] N. Bonanos, B.C.H. Steele, E.P. Butler, Applications of Impedance Spectroscopy, in: E. Barsoukov, J.R. Macdonald (Eds.), Impedance Spectroscopy, John Wiley & Sons, Inc., Hoboken, NJ, USA, 2005, pp. 205-537.

[71] A.S.A. Khiar, R. Puteh, A.K. Arof, Conductivity studies of a chitosan-based polymer electrolyte, Physica B 373(1) (2006) 23-27.

[72] S. Navaratnam, K. Ramesh, S. Ramesh, A. Sanusi, W.J. Basirun, A.K. Arof, Transport mechanism studies of chitosan electrolyte systems, Electrochim. Acta 175 (2015) 68-73.

[73] N.E. Suyatma, L. Tighzert, A. Copinet, V. Coma, Effects of Hydrophilic Plasticizers on Mechanical, Thermal, and Surface Properties of Chitosan Films, J. Agric. Food Chem. 53(10) (2005) 3950-3957.

Tables

Table 1. Sample codes and compositions (represented as portions by weight).

Sample	Chitosan	CMC	Glycerol	GO	rGO	2M Formic acid solution
AG2-F	100	–	20	–	–	261
AG2/GO-F	100	–	20	0.75	–	261
AG2/rGO-F	100	–	20	–	0.75	261
AG4-F	100		40	–	–	261
AG4/GO-F	100	–	40	0.75	–	261
AG4/rGO-F	100	–	40	–	0.75	261
BG2-F	50	50	20	–	–	261
BG2/GO-F	50	50	20	0.75	–	261
BG2/rGO-F	50	50	20	–	0.75	261
BG4-F	50	50	40	–	–	261
BG4/GO-F	50	50	40	0.75	–	261
BG4/rGO-F	50	50	40	–	0.75	261

Figure captions

Figure 1. STEM-HAADF images of the different biopolymer and composites films. Green arrows indicate non-dispersed particulate features (chitosan structure); yellow arrows indicate large-sized flocculent substances (GO or rGO nanosheets not fully exfoliated).

Figure 2. X-ray diffractograms for the different biopolymer and composite films: a) chitosan-based and b) chitosan/CMC-based. The reference lines indicate characteristic peaks for AG2-F.

Figure 3. FTIR spectra for the different biopolymer and composite films: a) chitosan-based and b) chitosan/CMC-based. The reference lines indicate characteristic bands of unprocessed CMC (1589 cm^{-1} and 1414 cm^{-1}) [27] and chitosan (the rest) [48]. The arrows indicate shifts in peak position or changes in peak intensity.

Figure 4. Derivative-weight-loss curves for the different biopolymer and composite films: a) chitosan-based and b) chitosan/CMC-based. The reference lines indicate the major peak temperatures of BG2-F and AG2-F, respectively.

Figure 5. Tan δ as a function of temperature for the different biopolymer and composite films: a) chitosan-based; b) chitosan/CMC-based.

Figure 6. EIS results for the different biopolymer and composite films: a) and b) Nyquist plot of impedance; c) and d) AC conductivity (σ); e) and f) real relative permittivity (ε'_r); and g) and h) imaginary electric modulus (M'').

Figure 7. a) and b) Representative stress–strain curves for the different biopolymer and composite films; c) Tensile strength, d) Young's modulus, and e) elongation at break of the different biopolymer and composite films. Error bars represent standard deviations.

Figure 8. Contact angle values for the different biopolymer and composite films at 0 s and 60 s. Error bars represent standard deviations.

Figure 9. Schematic representation of the effect of GO or rGO addition on chain interactions in the chitosan/CMC matrix.

Figures

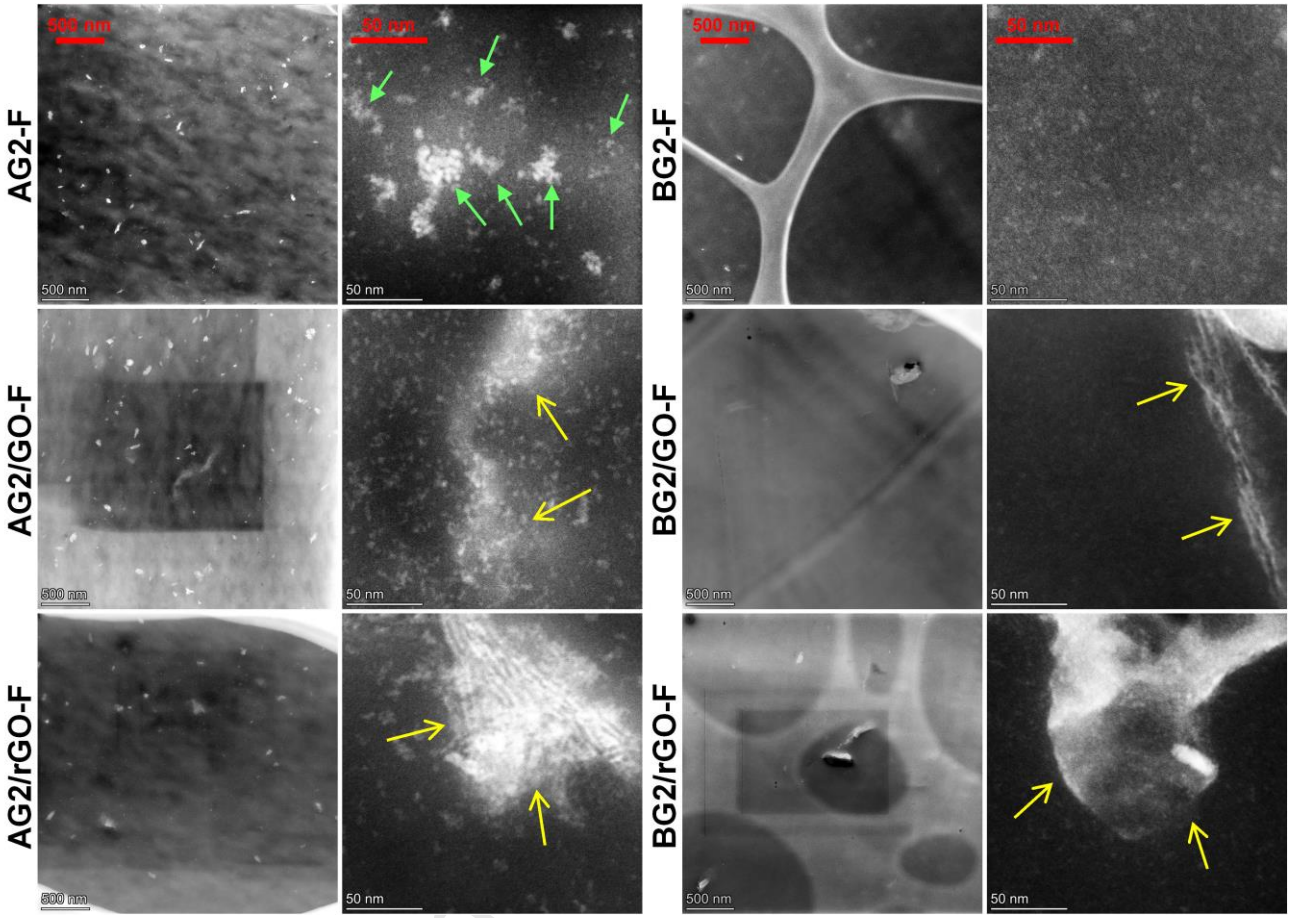

International Journal of Biological Macromolecules – Chen et al. – **Figure 1**

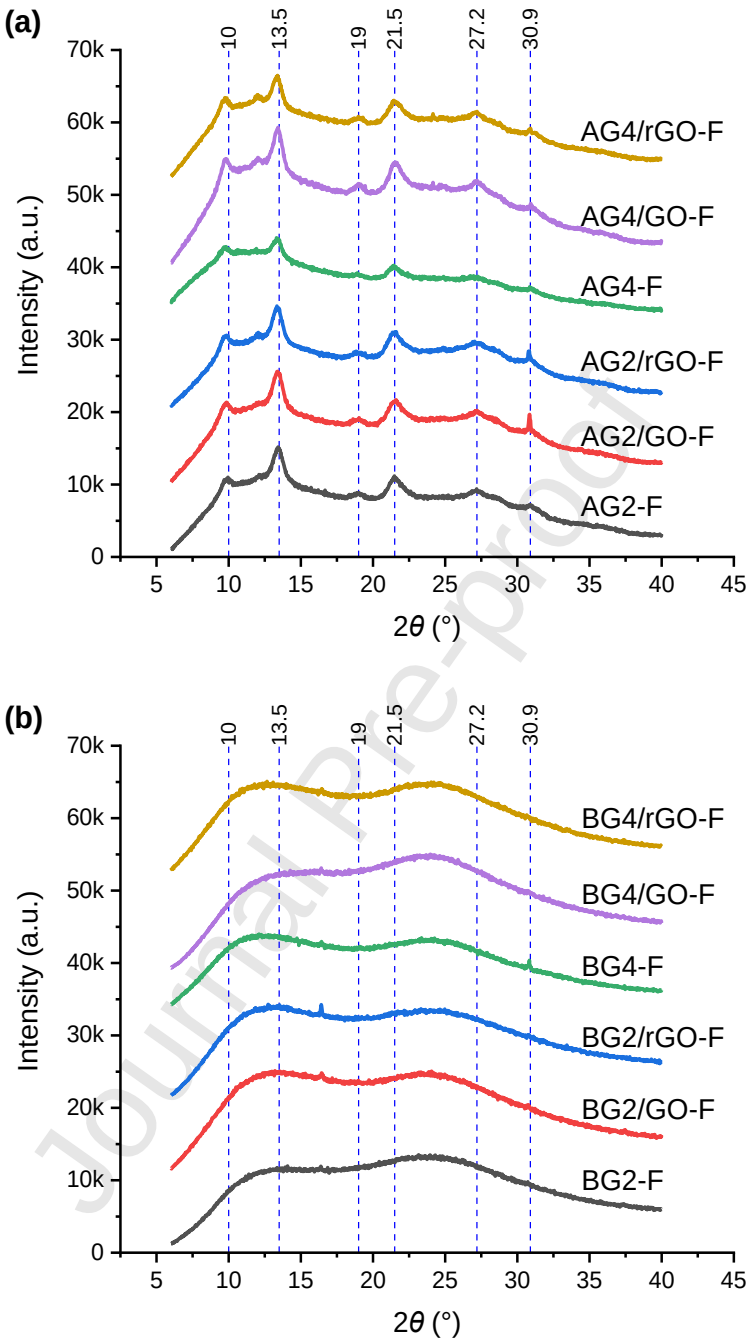

International Journal of Biological Macromolecules – Chen et al. – **Figure 2**

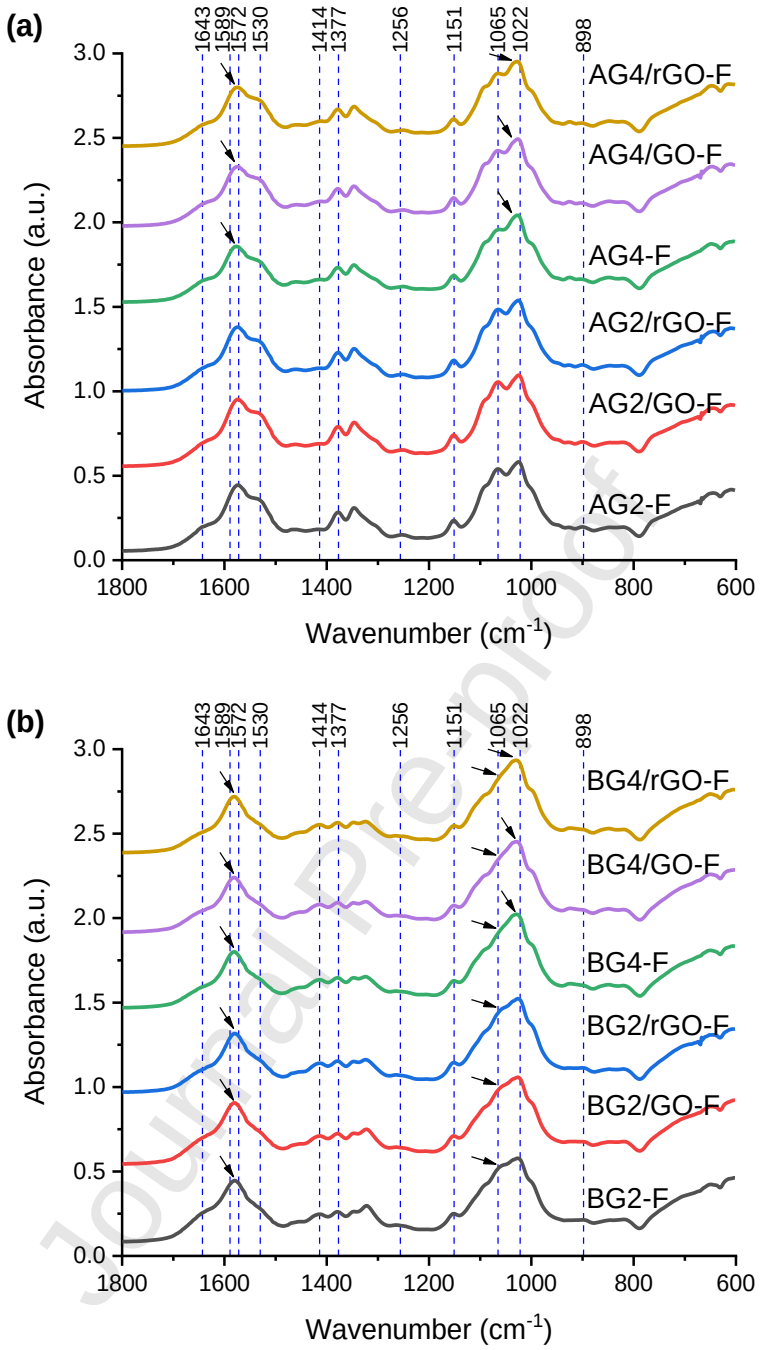

International Journal of Biological Macromolecules – Chen et al. – **Figure 3**

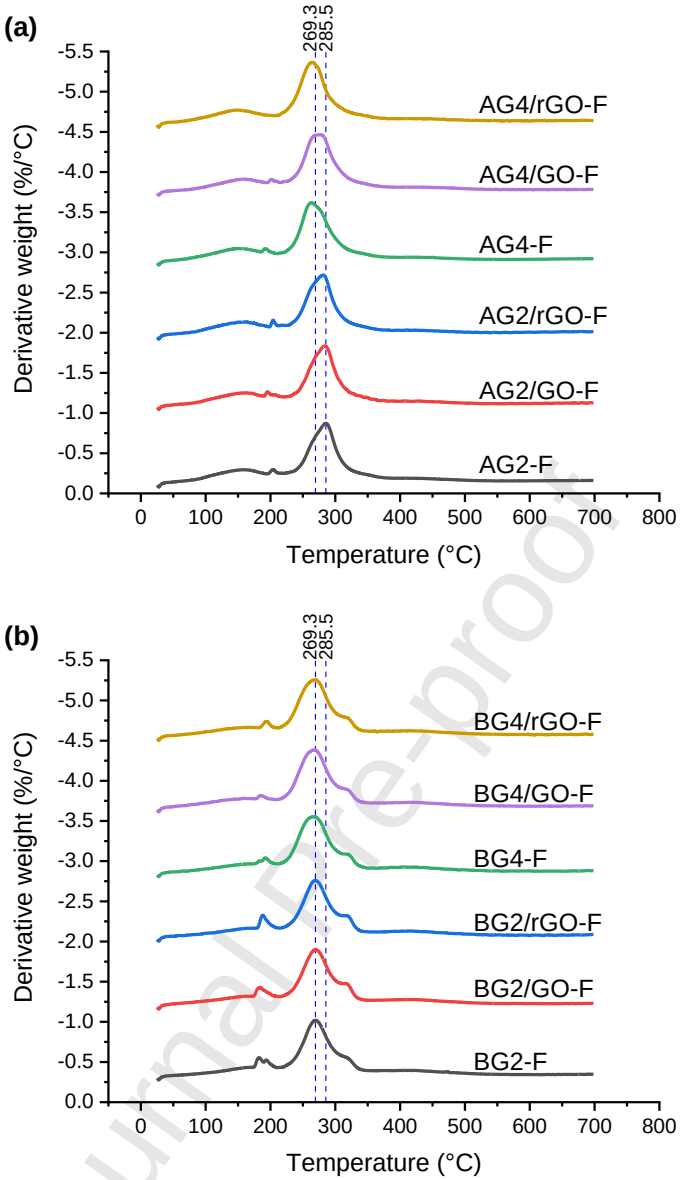

International Journal of Biological Macromolecules – Chen et al. – **Figure 4**

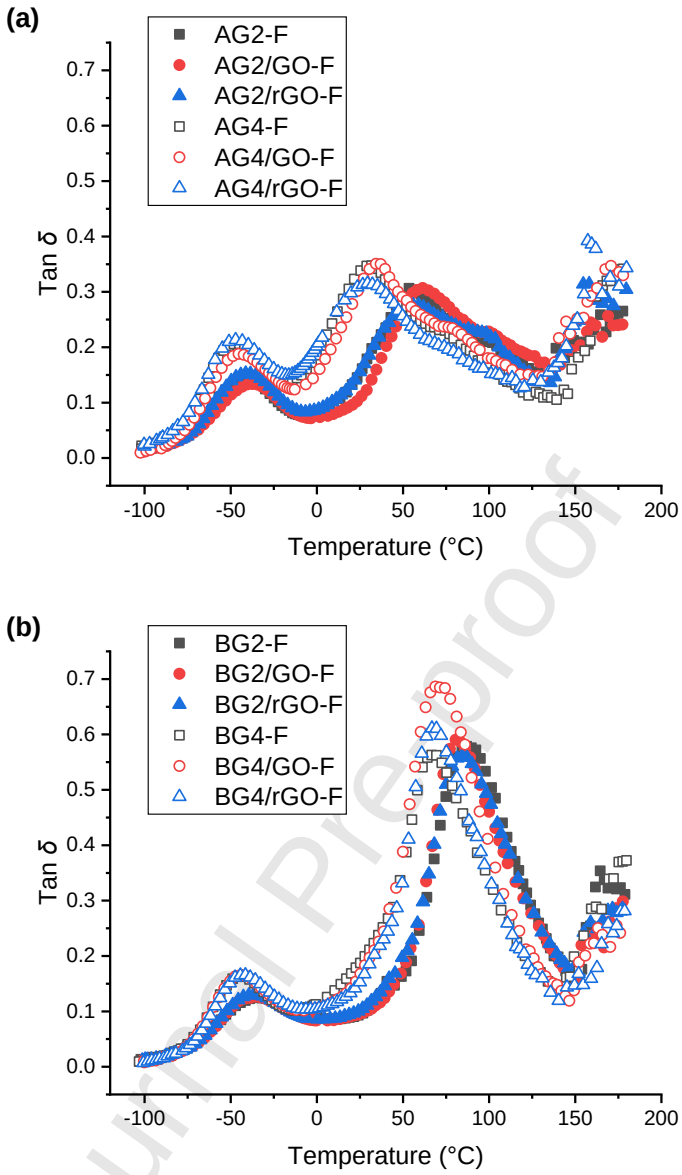

International Journal of Biological Macromolecules – Chen et al. – **Figure 5**

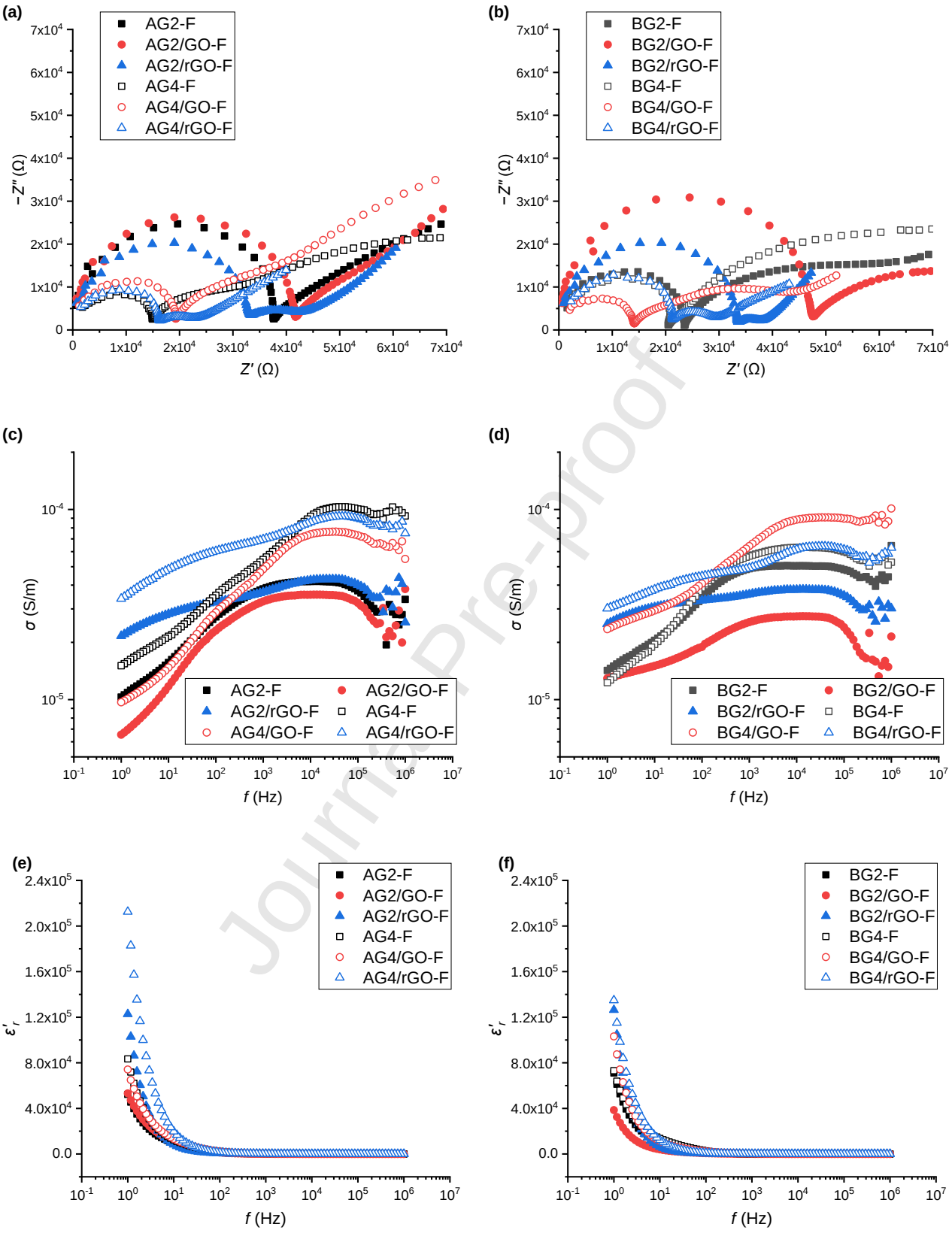

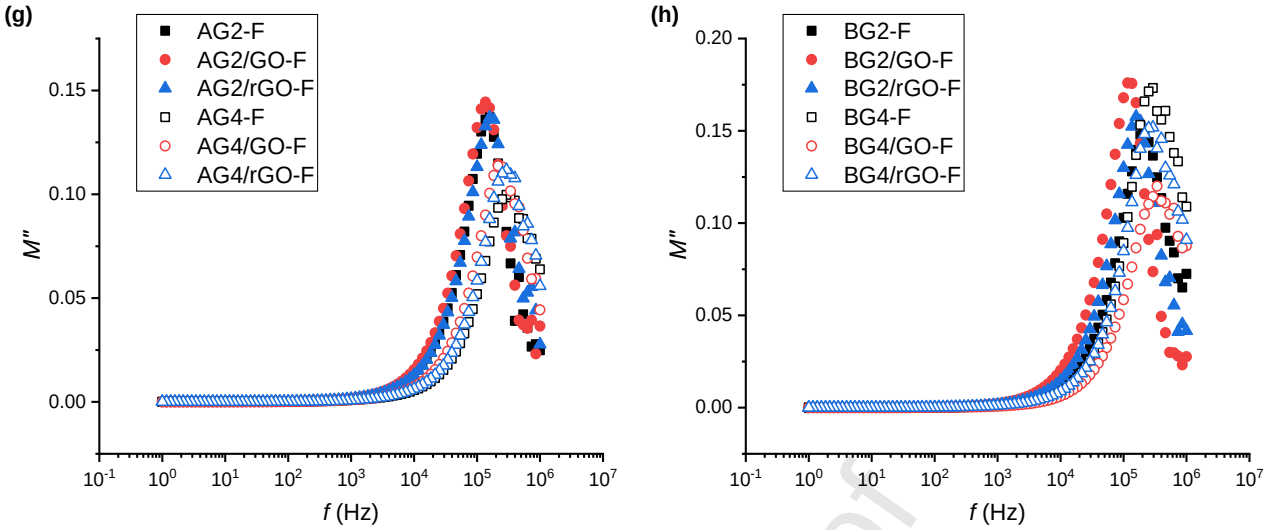

International Journal of Biological Macromolecules – Chen et al. – **Figure 6**

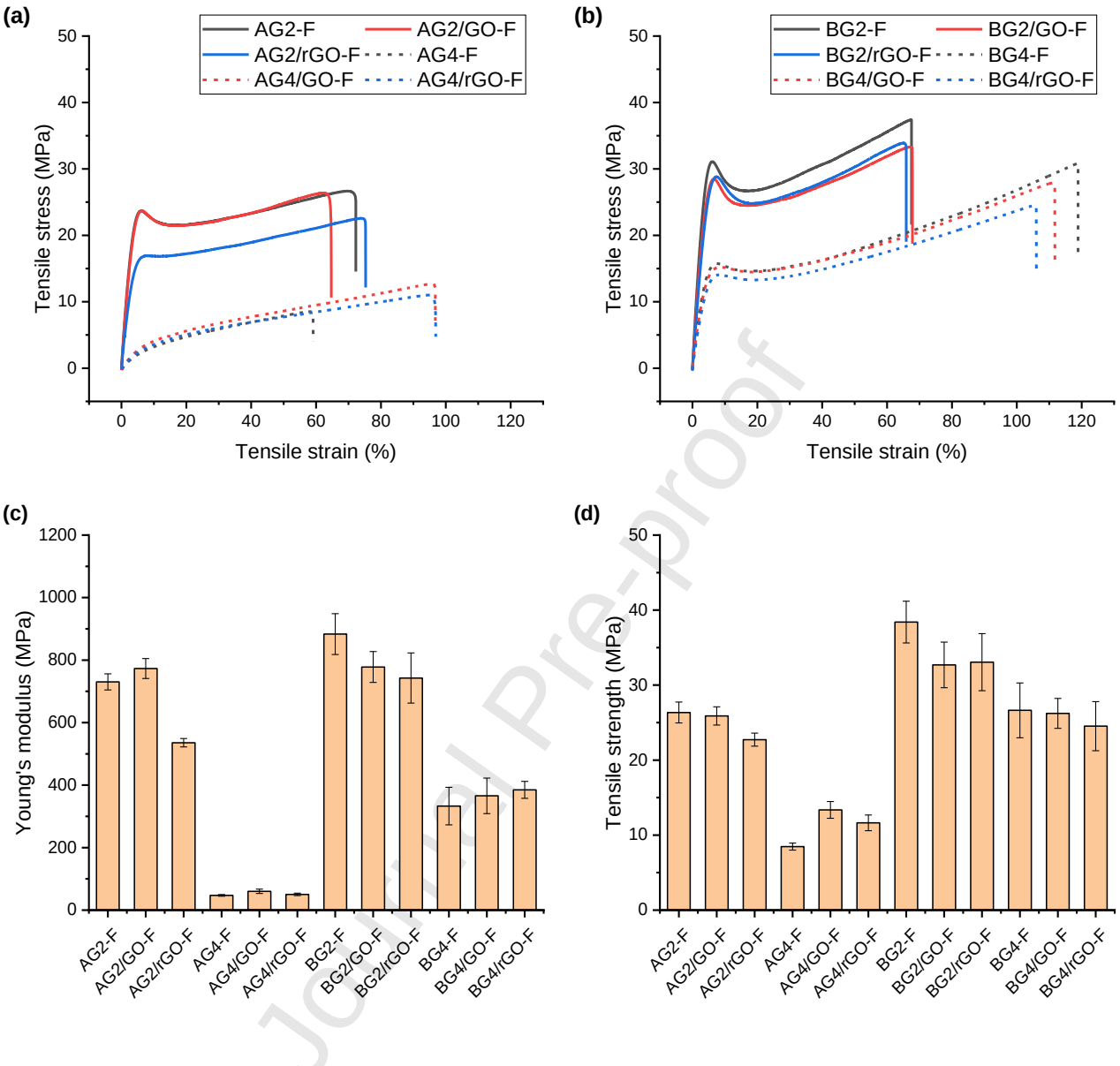

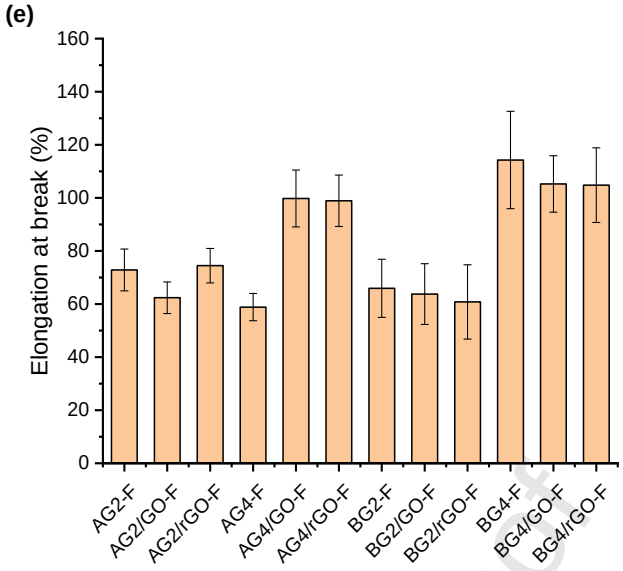

International Journal of Biological Macromolecules – Chen et al. – **Figure 7**

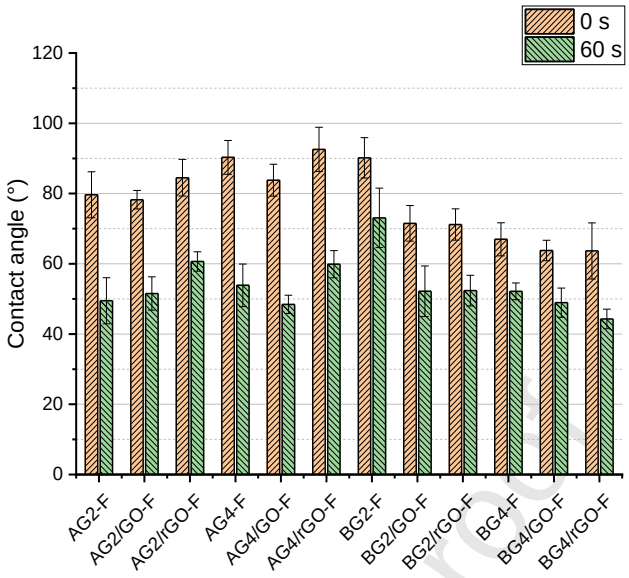

International Journal of Biological Macromolecules – Chen et al. – **Figure 8**

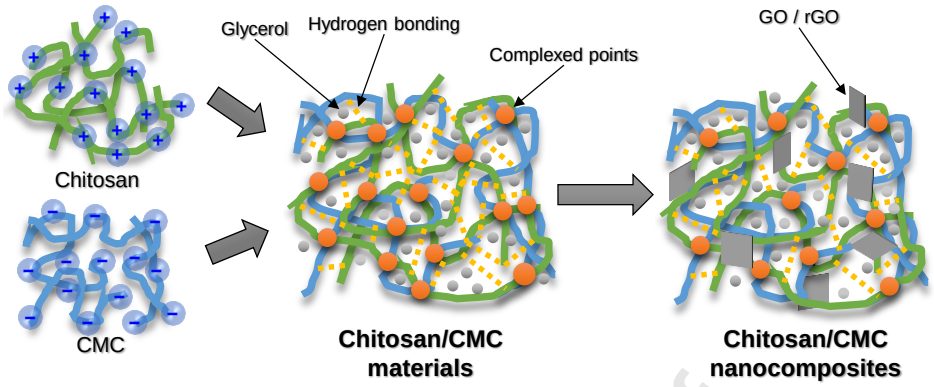

International Journal of Biological Macromolecules – Chen et al. – **Figure 9**

5 CRediT author statement:

Pei Chen: Methodology, Validation, Formal Analysis, Investigation. **Fengwei Xie:** Conceptualization, Methodology, Validation, Formal analysis, Investigation, Resources, Data Curation, Writing - Original Draft, Writing - Review & Editing, Visualization, Supervision, Project administration, Funding acquisition. **Fengzai Tang:** Investigation, Writing - Original Draft. **Tony McNally:** Conceptualization, Resources, Writing - Review & Editing, Supervision, Funding acquisition.

Graphical abstract

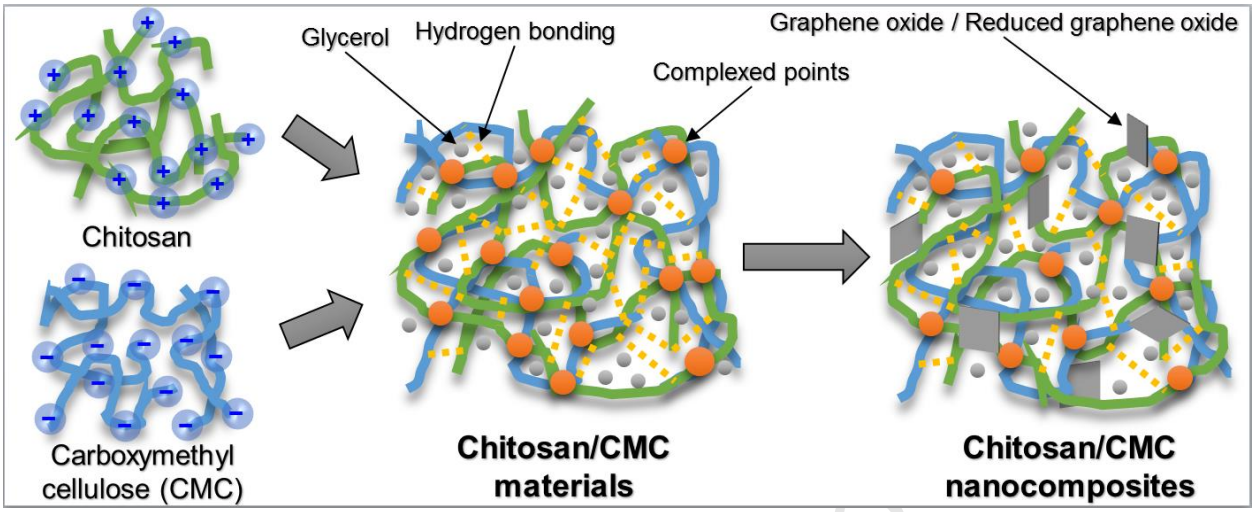

Highlights:

- ✓ Chitosan/carboxymethyl cellulose (CMC) nanocomposites thermomechanically processed
- ✓ Glycerol more important than GO/rGO to influence the nanocomposite characteristics
- ✓ GO/rGO might interfere with the polyelectrolyte complexation between biopolymers
- ✓ Some synergistic effects of glycerol and GO/rGO combined noticed
- ✓ Biopolymer nanocomposites showed high relative permittivity